JACS
JOURNAL OF THE AMERICAN CHEMICAL SOCIETY
Article
pubs.acs.org/JACS

# Electron Paramagnetic Resonance and Mössbauer Spectroscopy and Density Functional Theory Analysis of a High-Spin $Fe^{IV}$–Oxo Complex

Rupal Gupta,[†] David C. Lacy,[‡] Emile L. Bominaar,*[,†] A. S. Borovik,*[,‡] and Michael P. Hendrich*[,†]

[†]Department of Chemistry, Carnegie Mellon University, Pittsburgh, Pennsylvania 15213, United States
[‡]Department of Chemistry, University of California-Irvine, 1102 Natural Sciences II, Irvine, California 92697, United States

Supporting Information

**ABSTRACT:** High-spin $Fe^{IV}$–oxo species are known to be kinetically competent oxidants in non-heme iron enzymes. The properties of these oxidants are not as well understood as the corresponding intermediate-spin oxidants of heme complexes. The present work gives a detailed characterization of the structurally similar complexes $[Fe^{IV}H_3buea(O)]^-$, $[Fe^{III}H_3buea(O)]^{2-}$, and $[Fe^{III}H_3buea(OH)]^-$ ($H_3buea$ = tris[(*N*′-*tert*-butylureayla-to)-*N*-ethylene]aminato) using Mössbauer and dual-frequency/dual-mode electron paramagnetic resonance (EPR) spectroscopies. The $[Fe^{IV}H_3buea(O)]^-$ complex has a high-spin ($S = 2$) configuration imposed by the $C_3$-symmetric ligand. The EPR spectra of the $[Fe^{IV}H_3buea(O)]^-$ complex presented here represent the first documented examples of an EPR signal from an $Fe^{IV}$–oxo complex, demonstrating the ability to detect and quantify $Fe^{IV}$ species with EPR spectroscopy. Quantitative simulations allowed the determination of the zero-field parameter, $D = +4.7$ cm$^{-1}$, and the species concentration. Density functional theory (DFT) calculations of the zero-field parameter were found to be in agreement with the experimental value and indicated that the major contribution to the $D$ value is from spin–orbit coupling of the ground state with an excited $S = 1$ electronic configuration at 1.2 eV. $^{17}O$ isotope enrichment experiments allowed the determination of the hyperfine constants $^{17}O A_z = 10$ MHz for $[Fe^{IV}H_3buea(O)]^-$ and $^{17}O A_y = 8$ MHz, $^{17}O A_z = 12$ MHz for $[Fe^{III}H_3buea(OH)]^-$. The isotropic hyperfine constant ($^{17}O A_{iso} = -16.8$ MHz) was derived from the experimental value to allow a quantitative determination of the spin polarization ($\rho_p = 0.56$) of the oxo p orbitals of the Fe–oxo bond in $[Fe^{IV}H_3buea(O)]^-$. This is the first experimental determination for non-heme complexes and indicates significant covalency in the Fe–oxo bond. High-field Mössbauer spectroscopy gave an $^{57}Fe$ $\mathbf{A}_{dip}$ tensor of (+5.6, +5.3, −10.9) MHz and $A_{iso} = -25.9$ MHz for the $[Fe^{IV}H_3buea(O)]^-$ complex, and the results of DFT calculations were in agreement with the nuclear parameters of the complex.

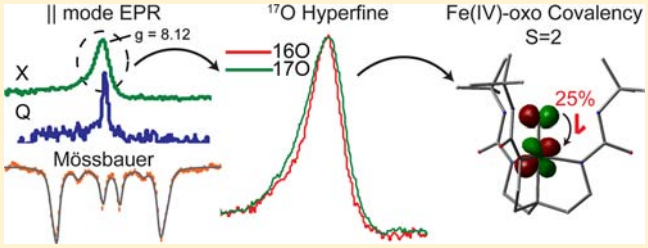


## INTRODUCTION

Dioxygen activation and substrate oxidation performed by metalloenzymes often involve high-valent reactive intermediates. The competent oxidants in several heme and non-heme iron enzymes are $Fe^{IV}$–oxo species. The reactivity of these $Fe^{IV}$–oxo centers is dependent on the reduction potential, spin state, and p$K_a$ of the metal–oxo moiety, the combination of which allows for the transformation of relatively stable bonds of substrates, such as the cleavage of C–H bonds.[1−4] In heme enzymes, the well-characterized Compound I and II intermediates involve an $Fe^{IV}$–oxo center,[5] and there is growing evidence in the literature for the role of $Fe^{IV}$–oxo units in the activity of non-heme iron enzymes.[6−8] In contrast to the intermediate-spin ($S = 1$) $Fe^{IV}$–oxo units of heme enzymes, the few non-heme enzymes for which an $Fe^{IV}$ species has been observed are high-spin ($S = 2$). For instance, a short-lived high-spin $Fe^{IV}$–oxo intermediate has been detected in taurine dioxygenase (TauD), an $\alpha$-ketoglutarate-dependent oxygenase.[9] This discovery led to the detection of other high-spin $Fe^{IV}$–oxo intermediates within $\alpha$-ketoglutarate-dependent enzymes, including halogenase SyrB2.[8]

Biomimetic complexes can be used to investigate the underlying chemistry of $O_2$ activation and substrate oxidation. These types of synthetic complexes can provide general insight into methods for detection and spectroscopic interpretation as well as the electronic properties of $Fe^{IV}$–oxo centers. Various synthetic non-heme $Fe^{IV}$–oxo complexes with tetragonal symmetry have been reported,[10,11] and they typically have an $S = 1$ ground state with a $d_{xy}^2 d_{xz}^1 d_{yz}^1$ electron configuration. The first example of a non-heme tetragonal $Fe^{IV}$–oxo complex with a high-spin ($S = 2$) ground state, arising from the weak ligand field of the pentaaquo coordination in $Fe^{IV}(H_2O)_5(O)$, was reported by Bakac and coworkers.[12] A high-spin configuration can also arise in trigonal symmetry provided that the two degenerate orbital pairs ($d_{xz}/d_{yz}$ and $d_{x^2-y^2}/d_{xy}$) are sufficiently close in energy. This suggestion is supported by two recent examples of high-spin $Fe^{IV}$–oxo complexes with ancillary tripodal ligands that support local $C_3$ symmetry.[13−15]

**Received:** April 3, 2012
**Published:** May 10, 2012

   dx.doi.org/10.1021/ja303224p | *J. Am. Chem. Soc.* 2012, 134, 9775−9784

The effects of the spin state on the reactivity of metal−oxo complexes have been addressed in a number of studies, and the possibility has been raised that high-spin $Fe^{IV}$−oxo complexes are more reactive than their low-spin counterparts.[17−24] However, in the case of hydrogen atom transfer, other determinants of reactivity may prevail.[25,26] Density functional theory (DFT) calculations and experimental measurements on $S = 1$ $Fe^{IV}$−oxo hemes suggest a significant degree of spin delocalization in the Fe−oxo bond. In view of the fact that the electron configurations of the $Fe^{IV}$−oxo units in the $S = 1$ state ($d_{xy}^2 d_{xz}^1 d_{yz}^1$) and the $S = 2$ state ($d_{xy}^1 d_{x^2-y^2}^1 d_{xz}^1 d_{yz}^1$) differ in the occupations of the in-plane $d_{xy}$ and $d_{x^2-y^2}$ orbitals but retain the occupations of the orbitals involved in the Fe−oxo bond, it would be expected that the spin delocalizations may be similar for heme and non-heme complexes. This paper presents the first experimental evidence to corroborate this expectation.

This report gives detailed electronic descriptions of Fe complexes of the ligand tris[(*N*′-*tert*-butylureaylato)-*N*-ethylene]aminato ($[H_3buea]^{3-}$). The equatorial anionic aminato N donors of the ligand enforce trigonal symmetry at the metal center. A rare attribute of this ligand set is the formation of intramolecular H-bonds by the butylureaylato arms with the axial oxygen. This ligand is capable of stabilizing a monomeric, high-spin $Fe^{IV}$−oxo complex, $[Fe^{IV}H_3buea(O)]^-$ (**1**), as well as its $Fe^{III}$−oxo and $Fe^{III}$−hydroxo analogues, $[Fe^{III}H_3buea(O)]^{2-}$(**2**) and $[Fe^{III}H_3buea(OH)]^-$ (**2-OH**), respectively (Figure 1).[13,16,27] The

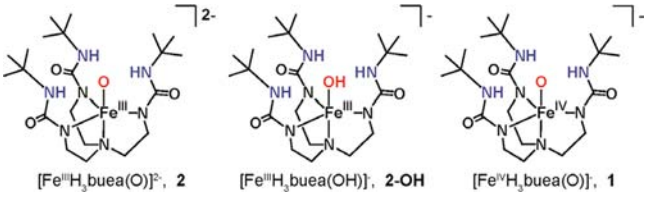


**Figure 1.** Structures of the $Fe^{III}$ and $Fe^{IV}$ complexes characterized in this report.[13,16]

$Fe^{III}$−oxo complex, which is the only known example of an $Fe^{III}$ unit with a terminal oxygen ligand, owes its stability to the protection offered by a network of intramolecular H-bonds provided by the ligand.[16] The structures of the three complexes have been characterized by X-ray diffraction (XRD) methods. In the present study, the electronic properties of these three complexes were examined using X- and Q-band, parallel- and perpendicular-mode electron paramagnetic resonance (EPR) spectroscopy, high-field Mössbauer spectroscopy, and DFT calculations. Isotopic $^{17}O$ labeling studies allowed a quantitative determination of the spin delocalization in the Fe−O bond, which is the first such experimental measurement for non-heme complexes. In addition, the present work demonstrates the utility of these methods for the characterization of Fe−oxo centers in metalloenzymes and biomimetic complexes.

## METHODS

**Preparation of $^{57}$Fe-Enriched Salts..**[28,29] The $^{57}$Fe source (metal foil, 94.69% enriched) was purchased from Pennwood Chemicals. For a typical synthesis, a small piece of metal foil (174 mg, 3.05 mmol) was immersed in dilute HCl and immediately poured onto a glass frit and washed with water. The metal was added to 3 mL of a 1:1 mixture of oxygen-free glacial acetic acid and acetic anhydride in a Schlenk tube, and the solution was then vigorously stirred and heated to ca. 90 °C under a $N_2$ atmosphere. After 24 h, the mixture contained a white precipitate and $^{57}$Fe metal. Volatiles were removed under reduced pressure, and the solid was isolated on a glass-fritted funnel under an argon atmosphere, washed thoroughly with $Et_2O$, and dried for several hours, after which the $^{57}$Fe metal was manually removed. The $^{57}Fe(OAc)_2$ obtained (35 mg, 6% yield) was used without further purification. This procedure was repeated several times with recycled $^{57}$Fe until enough solid was obtained to conduct the subsequent experiments. The $^{57}Fe(OAc)_2$ was used to prepare $K[^{57}Fe^{III}H_3buea(OH)]$, $K_2[^{57}Fe^{III}H_3buea(O)]$, and $K[^{57}Fe^{IV}H_3buea(O)]$ following literature procedures.[13]

**Preparation of $^{17}$O-Labeled Samples.** $^{17}$O-labeled water (60.6% enriched) was purchased from Icon Isotopes and used as received in the preparation of isotopically labeled samples. The $K[Fe^{III}H_3buea(^{17}OH)]$ salt was prepared following the literature procedure[13] using $H_2{}^{17}O$ as the source of the hydroxo ligand. The $K[Fe^{IV}H_3buea(^{17}O)]$ salt was isolated by treating $K[Fe^{III}H_3buea(^{17}OH)]$ with $[Fe^{III}Cp_2]BF_4$, following the literature procedure; $K_2[Fe^{III}H_3buea(^{17}O)]^{2-}$ was synthesized from the reaction of $K[Fe^{III}H_3buea(^{17}OH)]$ and $KOBu^t$.

**EPR Spectroscopy.** X-band EPR spectra were recorded on a Bruker 300 spectrometer equipped with an Oxford ESR-910 liquid helium cryostat. Q-band (34.0 GHz) EPR spectra were recorded on a Bruker 200 spectrometer with a home-built microwave probe and cryostat.[30] All of the signals were quantified relative to a CuEDTA spin standard. For both instruments, the microwave frequency was calibrated with a frequency counter and the magnetic field with an NMR gaussmeter. A modulation frequency of 100 kHz was used for all of the EPR spectra. The EPR simulation software (*SpinCount*) was written by one of the authors.[31] The software diagonalizes the spin Hamiltonian,

$$H = \beta_e \mathbf{B}\cdot\mathbf{g}\cdot\mathbf{S} + \mathbf{S}\cdot\mathbf{D}\cdot\mathbf{S} + \mathbf{S}\cdot\mathbf{A}\cdot\mathbf{I} \quad (1)$$

where **S** is the total spin of the complex (unless explicitly stated otherwise) and the parameters have the usual definitions. The quantitative simulations are least-squares fits of the experimental spectra generated with consideration of all of the intensity factors, which allows the computation of simulated spectra for a specified sample concentration.

**Mössbauer Spectroscopy.** Mössbauer spectra were recorded with two spectrometers using a Janis Research Super-Varitemp dewar. Isomer shifts are reported relative to Fe metal at 298 K. The simulations of Mössbauer spectra were calculated with least-squares fitting using the program *SpinCount* and the standard spin Hamiltonian

$$H = \beta_e \mathbf{B}\cdot\mathbf{g}\cdot\mathbf{S} + \mathbf{S}\cdot\mathbf{D}\cdot\mathbf{S} + \mathbf{S}\cdot\mathbf{A}\cdot\mathbf{I} - g_n b_n \mathbf{B}\cdot\mathbf{I} + \frac{eQV_{zz}}{12}\left[3I_z^2 - I(I+1) + \eta(I_x^2 - I_y^2)\right] \quad (2)$$

**DFT Calculations.** The DFT calculations were performed using the B3LYP hybrid functional and the 6-311G basis set provided by the Gaussian 03 software package (revision E.01).[32] Geometry optimizations were terminated upon reaching the default convergence criteria and were performed for **1** ($S = 1, 2$), **2** ($S = {}^5/_2$), and **2-OH** ($S = {}^5/_2$) without imposing any symmetry on the molecule. The optimizations of the structures for the $S = 1$ and $S = 2$ spin states of **1** were initiated using the crystal structure of **2**. Time-dependent DFT (TD-DFT) calculations were performed for the $S = 2$ and $S = 1$ states of **1** and the $S = {}^3/_2$ spin states of **2** and **2-OH**. The TD-DFT calculations gave positive excitation energies for all three complexes, suggesting that the self-consistent field (SCF) solutions represented the ground states. The vertical excitation energy calculations for the $S = 1$ state of **1** and the $S = {}^1/_2$ states of **2** and **2-OH** were performed using the equilibrium geometries of the $S = 2$ spin state of **1** and the $S = {}^5/_2$ states of **2** and **2-OH**. The dipolar hyperfine tensor ($\mathbf{A}_{dip}$) and the electric field gradient (EFG) tensor components ($V_{ii}$) were calculated using the keyword PROP. The quadrupole splitting ($\Delta E_Q$) and the symmetry parameter ($\eta$) were calculated from the EFG tensor components using the relations $\Delta E_Q = {}^1/_2 eQV_{zz}(1 + \eta^2/3)^{1/2}$ and $\eta = (V_{xx} - V_{yy})/V_{zz}$. The calculated isomer shifts ($\delta$) were obtained from the electron density at the nucleus and calculated using the calibrations of Vrajmasu et al.[33]


dx.doi.org/10.1021/ja303224p | *J. Am. Chem. Soc.* 2012, 134, 9775−9784

## RESULTS

**Spectroscopy of $Fe^{IV}$–Oxo Complex (1).** X- and Q- band measurements were performed on samples prepared by transferring aliquots of the same reaction mixture of **1** in *N*,*N*-dimethylformamide (DMF) to EPR tubes. The X-band spectrum, displayed in Figure 2A, shows a sharp signal at $g$ = 8.12 and a much broader signal at $g$ = 4.06. These signals originate from the $|2^{\pm}\rangle$ and $|1^{\pm}\rangle$ doublets, respectively, of an $S$ = 2 spin manifold, where the $|m^{\pm}\rangle$ nomenclature refers to the symmetric (+) and antisymmetric (−) combinations of the magnetic spin states (see the Discussion). The signals at $g$ = 4.30 and 2.00 are from a small amount (<1%) of adventitious $Fe^{III}$ and radical impurities. The presence of these weak signals in parallel mode was caused by a slight misalignment of the static and microwave magnetic fields. Plots of the signal intensity−temperature product (proportional to the population) versus temperature for the $g$ = 8.12 and 4.06 signals are shown in the lower inset of Figure 2. The signal at $g$ = 8.12 broadens for temperatures >40 K. The solid lines give the percent populations of the spin doublets calculated with eq 1 for $D$ = +4.0(5) $cm^{-1}$. The simulations overlaid on the data were generated with the parameters given in Table 1 and accurately match the signal shapes and intensities of both transitions as a function of temperature. The Q-band spectrum showed a signal at $g$ = 8.12 (Figure 2, upper inset) from the $|2^{\pm}\rangle$ doublet. The simulation using the same parameter set matches the Q-band spectrum. The intensity is in quantitative agreement with the concentrations of the sample determined from the molar absorptivity of the optical spectrum and from the absorption of an equivalent Mössbauer sample.

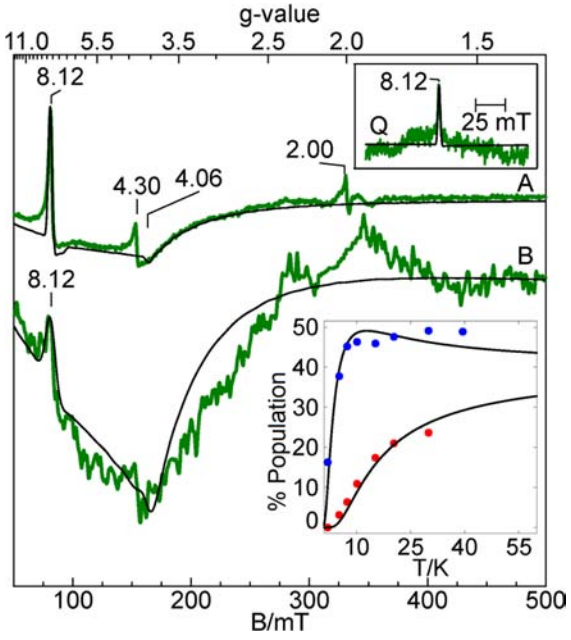


**Figure 2.** X-band EPR spectra of **1** in (A) DMF and (B) acetonitrile. The black lines are simulations with the parameters given in Table 1. Upper inset: Q-band EPR spectrum of **1** in DMF. Lower inset: plots of signal intensity−temperature product vs temperature for the $g$ = 4.06 (blue) and 8.12 (red) EPR signals of **1** recorded under nonsaturating conditions. The black lines, generated from the parameters in Table 1, give the theoretical percent populations of the magnetic sublevels of the $S$ = 2 manifold involved in the transitions as functions of temperature. The product of signal and temperature is proportional to the population of a specific doublet. Experimental conditions: microwave frequency, 9.3 GHz (X), 33.9 GHz (Q); power, 2 mW; temperature, 10 K; microwave mode, $\mathbf{B}_1 \parallel \mathbf{B}$.

The spectrum of **1** in acetonitrile (Figure 2B) illustrates the effect of solvent on the EPR spectrum of **1**. The spectra in Figure 2 have been scaled for equal concentration, showing that the intensity of the $g$ = 4.06 resonance grows significantly with the change in solvent to acetonitrile. The signal-to-noise ratio for the spectrum of **1** in acetonitrile is lower because of the lower concentration. The large increase in signal intensity at $g$ = 4.06 is due to a relatively small increase in the spread of $E/D$, as indicated by the parameter $\sigma_{E/D}$ (see the Discussion). The simulation in Figure 2B uses the same average zero-field parameters as in Figure 2A, but with an increase in $\sigma_{E/D}$ from 0.012 to 0.016. This simulation is also in quantitative agreement with the expected amount of the $Fe^{IV}$–oxo complex in the sample.

Equivalent samples of **1** containing $^{16}O$ or enriched in $^{17}O$ were prepared in 1:1 DMF/tetrahydrofuran (THF) from the oxidation of **2**-$^{16}$**OH** or **2**-$^{17}$**OH** (60% enriched). The parallel-mode EPR spectra of these samples (Figure 3) showed a broadening due to the $^{17}O$ isotope. The red and green simulations shown in Figure 3 were calculated with the parameters given in Table 1 in the absence and presence of an $^{17}O$ nucleus ($I$ = $^5/_2$) at 60% enrichment. The simulations reproduced the broadening with a hyperfine value of $^{17}A_z$ = 10 MHz. The spectrum is sensitive only to the $z$ component of the hyperfine tensor because the $|2^{\pm}\rangle$ doublet predominately magnetizes along this direction.

Low-temperature (4.2 K) Mössbauer spectra of an $^{57}Fe$-enriched sample of **1** in acetonitrile at various magnetic fields are shown in Figure 4. In a magnetic field of 50 mT (Figure 4G), the complex showed a single quadrupole doublet with $\delta$ = 0.020(5) mm/s and $\Delta E_Q$ = 0.43(3) mm/s. At higher fields, the complex displayed a magnetic hyperfine pattern. The simulation parameters given in Table 1 predicted the positions and intensities of all the features at 3 and 8 T (Figure 4A,B). However, at 0.5 and 1 T

**Table 1. Experimental and Calculated EPR and Mössbauer Parameters of 2, 2-OH, and 1**

| | 2 | | 2-OH | | 1 | |
|---|---|---|---|---|---|---|
| parameter | exptl | DFT | exptl | DFT | exptl | DFT |
| $D$ ($cm^{-1}$) | −0.7 | | −2.4 | | +4.7 | +3.9 |
| $E/D$, $\sigma_{E/D}$ | 0.005, 0.03 | | 0.157, 0.01 | | 0.03, 0.012 | |
| **g** | 2.00, 2.00, 2.00 | | 2.010, 2.009, 2.012 | | −, −, 2.02 | |
| $^{57Fe}\mathbf{A}^a$ | −24.8, −25.5, −24.4 | | −26.3, −28.4, −26.3 | | −20.3, −20.6, −37.0 | −21.3, −21.5, −35.2[b] |
| $\delta$ (mm/s) | 0.32 | 0.36 | 0.32 | 0.32 | 0.02 | 0.04 |
| $\Delta E_Q$ (mm/s) | −1.54 | −1.40 | −0.82 | +0.98 | +0.43 | +1.05 |
| $\eta$ | 0 | 0 | 0.65 | 0.74 | 0 | 0 |

[a] In MHz. [b] **A** tensor calculated by addition of the experimental $A_{iso}$ and the theoretical $\mathbf{A}_{dip}$.


dx.doi.org/10.1021/ja303224p | J. Am. Chem. Soc. 2012, 134, 9775−9784

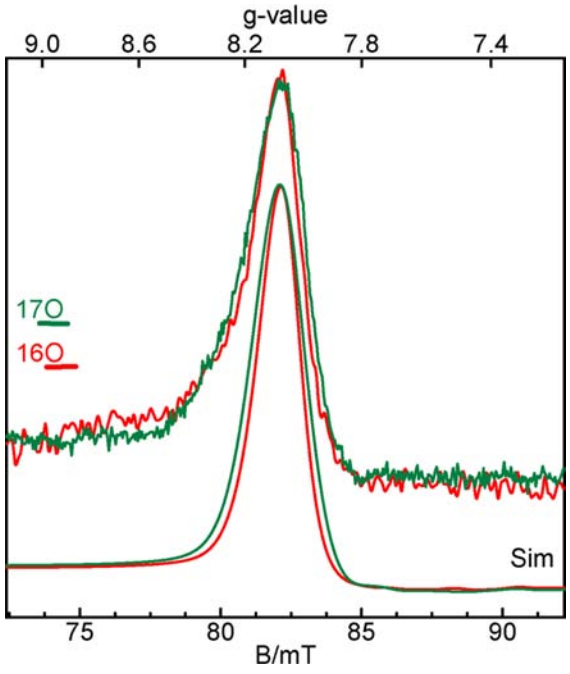


**Figure 3.** (top) EPR spectra and (bottom) simulations in the $g$ = 8 region for **1** containing $^{16}$O (red) or 60% enriched with $^{17}$O (green) in DMF/THF. The experimental conditions are the same as in Figure 2.

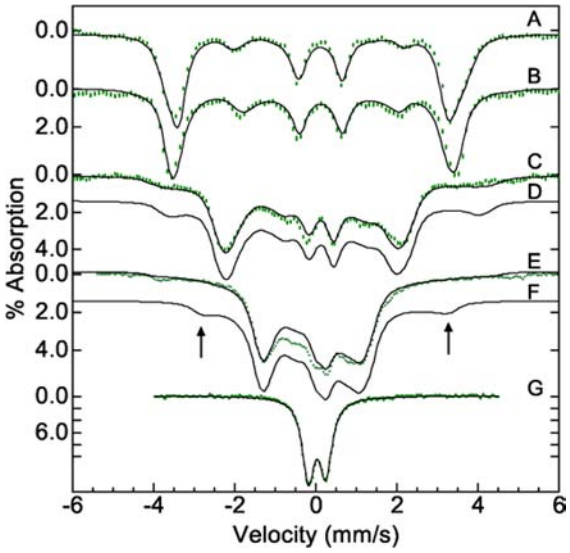


**Figure 4.** Mössbauer spectra of $^{57}$Fe-enriched **1** in acetonitrile in magnetic fields of (A) 8 T, (B) 3 T, (C) 1 T, (E) 0.5 T, and (G) 50 mT. The black traces are simulations using the parameters in Table 1. (D, F) Simulations of C and E, respectively, with $\sigma_{E/D}$ = 0. A high-spin ferric impurity, accounting for 12% of the Fe in the sample, was subtracted from all of the data except spectra E and G. The arrows indicate excited-state signals from the $m_S$ = −1 spin state. Experimental conditions: temperature, 4.2 K; magnetic field parallel to the $\gamma$-ray direction.

(Figure 4D,F), the same parameters predicted signals from the excited $m_S$ = −1 state (marked with arrows) that are not apparent in the experimental spectra. The simulations overlaid on the data include a distribution in $E/D$ ($\sigma_{E/D}$ = 0.016). This distribution had no effect on the 3 and 8 T simulations but broadened the $m_S$ = −1 feature beyond detection in the 0.5 and 1 T spectra (Figure 4C,E, black traces overlaid on the data). The same distribution was required for simulation of the EPR spectra, and the zero-field parameters used for the Mössbauer simulations are in agreement with those determined from EPR spectroscopy.

**Spectroscopy of Fe$^{III}$–Oxo Complex (2).** Figure 5A shows the EPR spectrum of **2** in DMF at 10 K. The signals at $g$ = 5.8 and

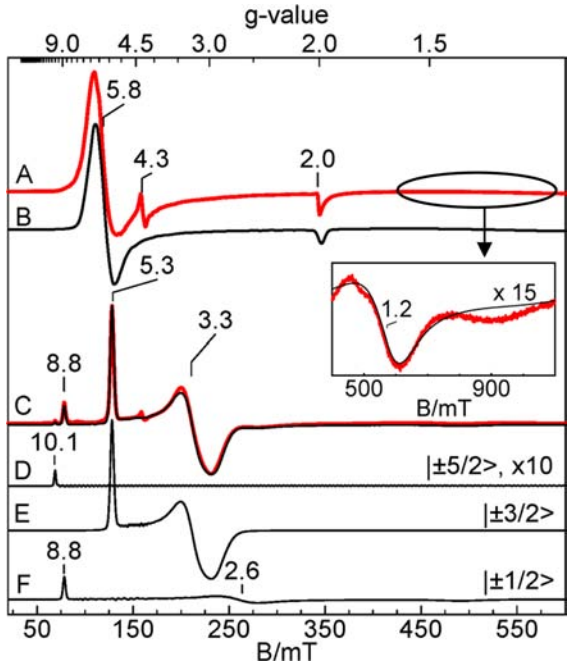


**Figure 5.** (A–C) EPR spectra (red) and simulations (black) of (A, B) **2** and (C) **2-OH** in DMF/THF. (D–F) Simulations for **2-OH** from transitions within the $m_S$ doublets $|\pm5/2\rangle$, $|\pm3/2\rangle$, and $|\pm1/2\rangle$. The black trace in C is the sum of D–F. Inset: High-field expanded view of **2** from the region indicated in A. Experimental conditions: microwave frequency, 9.64 GHz; power, 0.2 mW; temperature, 10 K; microwave mode, $\mathbf{B}_1 \perp \mathbf{B}$. The simulation parameters are given in Table 1.

2.0 are indicative of an axial high-spin ferric complex.[16,34] The signal at $g$ = 4.3 was from a small amount (<1%) of an Fe$^{III}$ impurity. Upon closer examination at higher field, an additional weak signal at $g$ = 1.2 was evident (Figure 5 inset). This signal is due to a $|\pm3/2\rangle$ transition, and its position and intensity were sensitive to the $D$ value. A fit to the temperature dependence of the $g$ = 5.8 signal indicated that it originated from an excited doublet, and together with the position of the $g$ = 1.2 resonance, the fit gave a $D$ value of −0.7(2) cm$^{-1}$. A simulation (Figure 5B and inset) with the parameters from Table 1 quantitatively agreed with the experimental spectrum. The simulations used a relatively large unresolved line width of 30 G, indicating the presence of intermolecular broadening. These intermolecular interactions are also believed to cause the asymmetric shape of the $g$ = 2 feature, which is not well predicted by the simulations. $^{17}$O enrichment of **2** showed no detectable broadening effects because the line widths of the signals are dominated by intermolecular interactions.

Figure 6 shows Mössbauer spectra of $^{57}$Fe-enriched **2** in *N*,*N*-dimethylacetamide (DMA) at 4.2 K in an applied magnetic field. At 50 mT (Figure 6B), the sample showed a superposition of two magnetic patterns originating from a 70:30 mixture of **2** and **2-OH**. It is difficult to prepare a pure solution of **2** without small amounts of **2-OH** impurity because of the strong basicity of the oxo group of **2** and residual acidic impurities present in the solvents. Figure 6A shows a spectrum of **2-OH** free of iron impurities. Figure 6C,D shows the difference spectra at 0.05 and


dx.doi.org/10.1021/ja303224p | J. Am. Chem. Soc. 2012, 134, 9775–9784

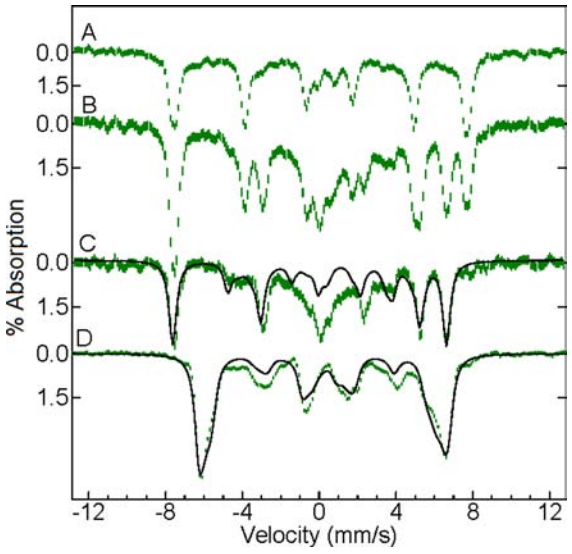


**Figure 6.** $^{57}$Fe Mössbauer spectra of **2** and **2-OH** in DMA in an applied magnetic field: (A) **2-OH** at 50 mT; (B) **2** at 50 mT; (C) difference spectrum (B − 0.3A); (D) difference spectrum for **2** at 8 T after subtraction of the **2-OH** spectrum. The black traces are simulations using the parameters in Table 1. The experimental conditions were the same as in Figure 5. The central region in spectrum C is from a small amount (<10%) of a diamagnetic impurity.

8 T after subtraction of the corresponding spectra of **2-OH** recorded under the same conditions. At 150 K (data not shown), the paramagnetic pattern did not collapse into a simple doublet, indicating that the electronic spin is in the intermediate relaxation regime. Simulations using the parameters given in Table 1 are overlaid on the data. The zero-field parameters are in agreement with those from the EPR analysis.

**Spectroscopy of Fe$^{III}$–Hydroxo Complex (2-OH).** An EPR spectrum of **2-OH** in DMF/THF is shown in Figure 5C. The complex exhibited sharp signals at $g$ = 10.1, 8.8, 5.3, 3.3, and 2.6 originating from the three $S = {}^5/_2$ doublets and indicative of a nonaxial ferric complex. The simulation (Figure 5C, black) using the parameters given in Table 1 quantitatively agrees with the experimental spectrum. Figure 5D–F shows the individual simulation for each doublet contributing to the spectrum (the quantum numbers in the $E/D$ = 0 limit are $m_S = \pm{}^5/_2, \pm{}^3/_2$, and $\pm{}^1/_2$, respectively). The relative intensities of the signals and their resonance positions allowed an accurate determination of $D$ and $E/D$ for the complex. The $g$ = 4.3 signal was from a minor amount (<0.1%) of an adventitious Fe$^{III}$ impurity.

Equivalent EPR samples of **2-OH** in DMF/THF were prepared with and without $^{17}$O enrichment (60%) of the hydroxo ligand. A magnified view of the EPR spectra in the region 10.5 < $g$ < 8.0 is shown in Figure 7. The $^{17}$O-labeled sample (Figure 7, green) showed broadening due to the $^{17}$OH$^-$ ligand when compared to **2-$^{16}$OH** (Figure 7, red). On the basis of simulations, the broadening due to $^{17}$O gave a hyperfine tensor of **A** = (n.d., 8, 12) MHz (n.d. = not determined) for the $^{17}$O nucleus. The signal at $g$ = 3.3 (Figure 5C,E) occurred for the molecular $x$ axis along the static magnetic field but was too broad to allow a determination of $A_x$.

Mössbauer spectra of an $^{57}$Fe-enriched sample of **2-OH** in DMA are shown in Figure 8. At 4.2 K and 50 mT (Figure 8A), the sample showed a six-line pattern indicative of a ferric species. As the applied magnetic field was increased from 3 to 8 T (Figure 8B and C, respectively), the six-line pattern moved inward because

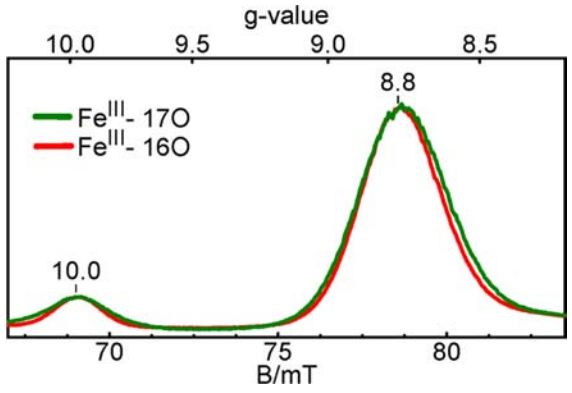


**Figure 7.** EPR spectra of **2-$^{16}$OH** (red) and **2-$^{17}$OH** (green) in DMF/THF. The experimental conditions were the same as in Figure 5.

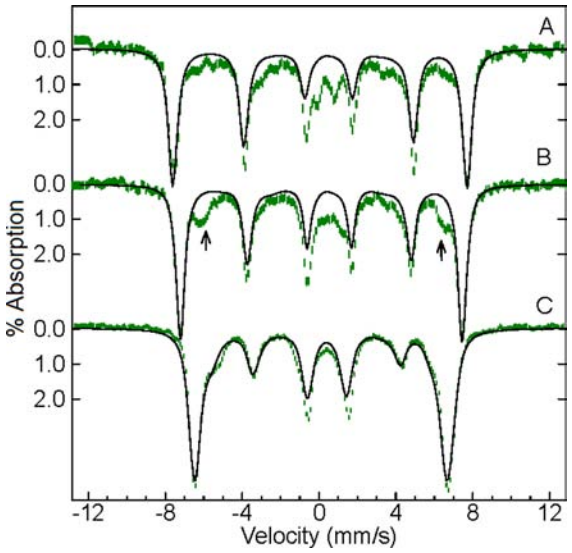


**Figure 8.** Mössbauer spectra of $^{57}$Fe-enriched **2-OH** in DMA in magnetic fields of (A) 50 mT, (B) 3 T, and (C) 8 T. The black traces are simulations using the parameters in Table 1. The arrows indicate signals from ferric impurity in the sample. The experimental conditions were the same as in Figure 4.

the external magnetic field opposed the internal magnetic field of the Fe nucleus. The features marked with arrows in the 3 T spectrum (Figure 8B) were due to a small amount of adventitious Fe in the sample. At 120 K, the six-line pattern collapsed to a doublet with $\delta$ = 0.32 mm/s and $\Delta E_Q$ = 0.82 mm/s. The simulations (Figure 8, black) were generated for an $S = {}^5/_2$ spin state using the parameters given in Table 1. The parameters from the simulation of the EPR and Mössbauer data are in agreement.

**DFT Studies.** The DFT-optimized structure for the $S$ = 2 state of **1** is in good agreement with the crystal structure, as indicated by a comparison of the selected bond distances and angles in Table 2. The table also presents data for the optimized structure of the $S$ = 1 state. As expected from the orbital occupancies in the two spin states, the three Fe–N$_{eq}$ distances are virtually equal in the $S$ = 2 structure but are not equal in the $S$ = 1 structure. On average, the Fe–N$_{eq}$ distances in the $S$ = 2 structure $[(d_{xz}/d_{yz})^2(d_{xy}/d_{x^2-y^2})^2]$ are 0.09 Å longer than those in the $S$ = 1 structure $[(d_{xz}/d_{yz})^3(d_{xy}/d_{x^2-y^2})^1]$, whereas the Fe–O and Fe–N$_{ax}$ distances in the $S$ = 2 structure are shorter by 0.03 and 0.10 Å, respectively. Like **1**, DFT optimizations gave **2** and **2-OH** structures in good agreement with the XRD data. The


dx.doi.org/10.1021/ja303224p | J. Am. Chem. Soc. 2012, 134, 9775–9784

Table 2. Comparison of Calculated and Experimental Values of Selected Bond Distances (Å) and Angles (deg) in **1** and $[Fe^{IV}(TMG_3tren)(O)]^{2+}$

| | | **1** (DFT) | | |
|---|---|---|---|---|
| | **1** (X-ray) | $S = 2$ | $S = 1$ | TMG[a] (X-ray) |
| Fe−O | 1.680 | 1.677 | 1.706 | 1.661 |
| Fe−$N_{eq}$1 | 1.981 | 1.999 | 1.874 | 1.994 |
| Fe−$N_{eq}$2 | 1.988 | 2.001 | 1.932 | 2.006 |
| Fe−$N_{eq}$3 | 1.997 | 2.001 | 1.933 | 2.020 |
| avg Fe−$N_{eq}$ | 1.989 | 2.000 | 1.913 | 2.005 |
| Fe−$N_{ax}$ | 2.064 | 2.105 | 2.211 | 2.121 |
| avg O−Fe−$N_{eq}$ | 97.59 | 97.44 | 98.55 | 97.81 |

[a] $[Fe^{IV}(TMG_3tren)(O)]^{2+}$.

DFT values for the spectroscopic parameters obtained for the optimized structures of **1**, **2**, **2-OH** are presented in Table 1.

## DISCUSSION

**Spectroscopy of $Fe^{IV}$−Oxo Complex (1).** The catalytic cycles of the non-heme α-ketoglutarate-dependent oxygenase and halogenase enzymes involve high-spin $Fe^{IV}$−oxo intermediates.[8,9] The present work demonstrates that high-spin $Fe^{IV}$−oxo species can be characterized with EPR spectroscopy. The software we have developed allows the spin concentration to be determined directly from EPR spectra. The ability to detect and quantify such EPR signals is an important advance for kinetic and mechanistic studies aimed at quantifying the intermediates formed during the reaction cycles of biomimetic and enzymatic systems.

$Fe^{IV}$−oxo complex **1** showed signals from transitions within the $|1^{\pm}\rangle$ and $|2^{\pm}\rangle$ doublets of the $S = 2$ spin manifold. The detection of signals from both doublets of an $S = 2$ state is rare. For integer-spin systems with near-axial symmetry, the non-Kramers states in zero magnetic field are approximately the symmetric and antisymmetric combinations of the $m_S$ states: $|m^{\pm}\rangle = (|+m\rangle \pm |-m\rangle)/\sqrt{2}$, where $m = 1$ or 2.[35] The resonance condition for these doublets is $(h\nu)^2 = \Delta_m^2 + (g_z\beta B \cos\theta)^2$, where $\theta$ is the angle between the molecular $z$ axis and the external field (**B**) and the zero-field splittings of the two doublets are $\Delta_1 = 6E$ and $\Delta_2 = 3D(E/D)^2$. The signal intensity from transitions within each doublet is proportional to $\Delta_m^2$. For **1**, the ratio $\Delta_2/\Delta_1 = 67$ implies that the signal from the $|1^{\pm}\rangle$ transition would be a factor of 4500 more intense than the signal from the $|2^{\pm}\rangle$ transition. However, the distribution of $\Delta_m$ values is significantly greater for the $|1^{\pm}\rangle$ transition. The distribution of $\Delta_1$ is shown in Figure S2 in the Supporting Information. The center of the distribution is at 0.83 $cm^{-1}$, meaning that a large fraction of molecules have $\Delta_1 > h\nu = 0.3$ $cm^{-1}$ (X band) and cannot satisfy the resonance condition. As the width of the distribution of $E/D$ increases, a greater fraction of molecules can satisfy the resonance condition, resulting in increased signal intensity. This is evident from the comparison of the EPR data for **1** in DMF and acetonitrile. The solvent interactions in acetonitrile induce a wider distribution of $E/D$ ($\sigma_{E/D} = 0.016$) than in DMF ($\sigma_{E/D} = 0.012$), resulting in a greater fraction (11 vs 6%) of molecules with $\Delta_1 < h\nu$ and thus a higher intensity for the resonance in acetonitrile. The average value of $\Delta_1$ is less than the microwave quantum at the Q band (1.2 $cm^{-1}$), so a majority of molecules can be brought into resonance. Despite the larger fraction, the simulations indicated that the distribution severely broadens the signal, rendering it undetectable against the baseline. For the $|2^{\pm}\rangle$ doublet of **1**, the distribution of $\Delta_2$ is sharp and entirely less than the microwave energy, resulting in a detection limit for **1** of 0.5 mM. Enzymatic active sites are expected to have lower symmetry and higher $E/D$ values, and since the intensity is proportional to $(E/D)^4$, it is anticipated that the detection limit will decrease significantly for metalloenzymes (i.e., ≪0.5 mM).

The $^{57}$Fe isomer shift for **1** (0.02 mm/s) is significantly lower than the corresponding values for other $S = 2$ $Fe^{IV}$−oxo species, including TauD-**J** (the $Fe^{IV}$−oxo intermediate of TauD), and the synthetic complexes $Fe^{IV}(H_2O)_5(O)$ and $[Fe^{IV}(TMG_3tren)(O)]^{2+}$ ($\delta$ = 0.3, 0.38, and 0.09 mm/s, respectively).[12,14] The lower magnitude of the isomer shift in **1** indicates higher covalency of the Fe−$N_{eq}$ bonds, resulting in a higher s-electron density at the iron nucleus. This is consistent with the overall shorter Fe−N bond lengths in **1** relative to those in the $[Fe^{IV}(TMG_3tren)(O)]^{2+}$ complex (Table 2). The Fe−oxo bond of **1** is longer, presumably because of the hydrogen bonding present in **1**, as discussed below. The $^{57}$Fe **A** tensor of **1** is similar to those of other high-spin $Fe^{IV}$ complexes (Table 3). The isotropic value ($A_{iso}$) for **1** is −25.9 MHz, while those for $Fe^{IV}(H_2O)_5(O)$, TauD-**J**, and $[Fe^{IV}(TMG_3tren)(O)]^{2+}$ are −34, −30.6, and −26.6 MHz, respectively.[9,12,14,36] The order of the $|A_{iso}|$ values for the series, $Fe^{IV}(H_2O)_5(O)$ > TauD-**J** > $[Fe^{IV}(TMG_3tren)(O)]^{2+}$ > **1**, also reflects an increase in covalency and reduction of the spin polarization of the s electrons by the d electrons, consistent with the trend deduced from the isomer shift. The anisotropic dipolar hyperfine tensor for **1** is $\mathbf{A}_{dip}$ = (+5.6, +5.3, −10.9) MHz, which is within 5% of the values for $[Fe^{IV}(TMG_3tren)(O)]^{2+}$ and TauD-**J** (Table 3). The three complexes have axial $\mathbf{A}_{dip}$ tensors with similar principal values, as they all have a strongly coordinating oxo ligand. The dipolar **A** tensor of **1** predicted by DFT calculations is (+4.7, +4.5, −9.2) MHz, which is in reasonable agreement with the experimental measurement.

**$^{17}$O Hyperfine Interaction and Fe−Oxo Bond Covalency.** The EPR resonance at $g = 8.12$ is sufficiently sharp to allow detection of broadening from $^{17}$O isotopic enrichment. A large broadening of a $g = 8$ signal due to $^{17}$O was recently observed for an $Fe^{III}$−superoxo species in a catechol dioxygenase. The broadening allowed the measurement of a component of

Table 3. Comparison of EPR and Mössbauer Parameters of Selected $S = 2$ $Fe^{IV}$−Oxo Complexes

| complex | $D$[a] | $E/D$ | $\delta$[b] | $\Delta E_Q$[b] | $^{57}\mathbf{A}_{dip}$[c] | $^{57}A_{iso}$[c] | ref |
|---|---|---|---|---|---|---|---|
| $[Fe^{IV}H_3buea(O)]^-$ | +4.7 | 0.03 | 0.02 | 0.43 | +5.6, +5.3, −10.9 | −25.9 | this work |
| $[Fe^{IV}(TMG_3tren)(O)]^{2+}$ | +5.0 | 0.02 | 0.09 | −0.29 | +5.4, +6.4, −11.8 | −26.6 | 14 |
| TauD-**J** | +10.5 | 0.01 | 0.31 | −0.88 | +5.4, +6.5, −11.9 | −30.6 | 9 |
| $[Fe^{IV}(H_2O)_5(O)]^{2+}$ | +9.7 | 0 | 0.38 | −0.33 | −34.0 | −34.2[d] | 12 |
| $[Fe^{IV}(tpaPh)(O)]^-$ | +4.32 | 0.098 | 0.09 | 0.51 | n.d. | n.d. | 15 |

[a] In $cm^{-1}$. [b] In mm/s. [c] In MHz. [d] The value for this complex was calculated from the two experimental $A$ values and the dipolar **A** tensor obtained from DFT calculations.


dx.doi.org/10.1021/ja303224p | J. Am. Chem. Soc. 2012, 134, 9775−9784

the $^{17}$O**A** hyperfine tensor, which was found to be large and indicative of localization of an unpaired electron on the superoxide.[37] The $^{17}$O-enriched samples of **1** in the present study showed much less broadening. Nevertheless, as described next, this result is indicative of significant oxo spin polarization and covalency resulting from binding to the paramagnetic Fe$^{IV}$ ion.

The $^{17}$O magnetic hyperfine interaction is described by the Hamiltonian $^{17}$O**I**·$^{17}$O**A**·**S**, where **S** is the spin of the iron center. Except where explicitly stated otherwise, the $A$ values are given for a Hamiltonian with $S = 2$ for **1** or $S = {}^5/_2$ for **2** or **2-OH**. The isotropic hyperfine constant ($^{17}O_{iso}$) of $^{17}$O can be expressed as[38]

$$^{17}O_{iso} = a_p\rho_p = {}^{17}O_z - {}^{17}O_{dip,z} \quad (3)$$

This assumes that $^{17}O_{iso}$ is proportional to $\rho_p$, the spin population of the p orbitals of the oxo ligand ($\rho_p = \rho_{p_x} + \rho_{p_y} + \rho_{p_z}$). The constant $a_p$ is the isotropic hyperfine coupling for an unpaired electron in a p orbital of oxygen ($\rho_p = 1$). The magnitude of $\rho_p$ is indicative of the delocalization of the oxygen p electrons into the Fe d orbitals, which gives rise to spin polarization on the oxo ligand. For example, $\rho_p = 0$ would correspond to an ionic Fe$^{IV}$–O$^{2-}$ bond (no delocalization), whereas $\rho_p = 1$ would correspond the transfer of a net amount of electron spin density representing one unpaired electron. In eq 3, $^{17}O_{dip,z}$ is the $z$ component of the dipolar hyperfine tensor, $\mathbf{A}_{dip}$. The simulation of the $g = 8.12$ resonance gave an experimental value of $^{17}O_z = \pm 10$ MHz (see Figure 3 and the Results). This resonance is sensitive only to the component of the **A** tensor along the Fe–oxo bond (the molecular $z$ axis), and the sign of hyperfine values cannot be determined by EPR spectroscopy. DFT calculations of Fe$^{IV}$–oxo species with the functional and basis set adopted here have the propensity to underestimate the s-orbital polarization of the electrons at the iron nucleus, giving a lower magnitude of $^{57}$Fe$A_{iso}$ than the experimental value. The analysis presented below suggests that a similar problem arises for $^{17}O_{iso}$. In contrast to the isotropic value, the $\mathbf{A}_{dip}$ tensor can be calculated with reasonable accuracy. DFT calculations on the optimized structure gave $^{17}\mathbf{A}_{dip}$ = (−13.4, −13.4, +26.8) MHz and $^{17}O_{iso}$ = −11 MHz for the $^{17}$O isotopologue. With the DFT value of +26.8 MHz for $^{17}O_{dip,z}$ and the experimental $A_z$ value of ±10 MHz, eq 3 gave two possible values for $^{17}O_{iso}$: −16.8 or −36.8 MHz. The value $a_p^{S=1/2} = -120$ MHz has been reported previously for a single unpaired electron in an oxygen p orbital.[38,39] This value can be converted to that appropriate for an $S = 2$ Hamiltonian as $a_p = a_p^{S=1/2}/4 = -30$ MHz.[38,40] The value of the total unpaired spin density, $\rho_p$, in the oxo 2p orbitals can then be solved using eq 3 and the two values of $^{17}O_{iso}$ to give $\rho_p = 0.56$ ($^{17}O_{iso} = -16.8$ MHz) or 1.23 ($^{17}O_{iso} = -36.8$ MHz). The value of $\delta$ and the $^{57}$Fe **A** tensor obtained from Mössbauer spectroscopy were in the range expected for the +4 oxidation state of Fe, favoring the value $\rho_p = 0.56$. The value $\rho_p = 1.23$ would be expected to give a +3 oxidation state of Fe. Furthermore, the Mulliken spin populations for the $d_{xz}$ and $d_{yz}$ orbitals calculated by DFT are equal to 1.25 (Table S1 in the Supporting Information). The total spin density transferred from the oxo $p_x/p_y$ orbitals into the Fe $d_{xz}/d_{yz}$ orbitals is $2(1 - 1.25) = -0.5$, resulting in spin populations of +0.25 in each of the $p_x$ and $p_y$ orbitals of oxygen. Thus, the Mössbauer data and the Mulliken population analysis are most consistent with the value of $\rho_p = 0.56$. This large value of the spin polarization of the oxo ligand indicates significant covalency of the Fe–oxo bond. $^{17}$O electron–nuclear double resonance (ENDOR) studies of horseradish peroxidase Compound I have estimated a delocalization of 25% for the $S = 1$ Fe$^{IV}$–O heme center,[41] yielding a net spin population of $\rho_p = 2 \times 0.25 = 0.50$ shared between $p_x$ and $p_y$, which is comparable to the net spin population of **1**.

Recent work has determined that the Fe$^{III}$–superoxo species of catechol dioxygenase has nearly a full unpaired electron localized on the superoxo ligand, with a correspondingly large $^{17}$O hyperfine value.[37] The rather small $^{17}$O broadening effect observed for **1** was unexpected given the significant spin polarization of $\rho_p = 0.56$. The small hyperfine value observed for **1** is a consequence of two factors: the lower overall spin polarization and the O p-orbital occupations. For superoxide, the localization of an unpaired electron in a single $\pi^*$ orbital gives (for $S = {}^1/_2$) $^{17}\mathbf{A}_{dip}^{S=1/2} = (-160, +80, +80)$ MHz.[42] In contrast, for **1**, the singly occupied Fe $d_{xz}$ and $d_{yz}$ orbitals form $\pi$ bonds with the oxo $p_x$ and $p_y$ orbitals, inducing polarization of the electron spin in both oxo orbitals. The two orbital polarization changes the sign of the largest component of $^{17}\mathbf{A}_{dip}$ to give (for $S = {}^1/_2$) $^{17}\mathbf{A}_{dip}^{S=1/2} = (-54, -54, +108)$ MHz. For both the Fe$^{III}$–superoxo species of catechol dioxygenase and **1**, the EPR resonance is sensitive to the largest component of $^{17}\mathbf{A}_{dip}$. For the Fe$^{III}$–superoxo species, the largest component (−160 MHz) has the same sign as $A_{iso}$. In contrast, for **1** the sign of the largest component (+108 MHz) is opposite that of $A_{iso}$, and consequently, the two values effectively cancel, giving the small $A$ value observed experimentally.

**DFT Calculations on 1.** The DFT-optimized structure of **1** gives the d-orbital scheme shown in Figure S1 in the Supporting Information, with an electron configuration of $d_{xz}^1 d_{yz}^1 d_{xy}^1 d_{x^2-y^2}^1$. The trigonal symmetry results in degeneracy of the $d_{xz}$ and $d_{yz}$ orbitals, which are lower in energy than the degenerate set consisting of the $d_{xy}$ and $d_{x^2-y^2}$ orbitals. The Fe ion is displaced above the plane formed by the equatorial nitrogens ($N_{eq}$), as is evident from the average O–Fe–$N_{eq}$ angle of 97.5°. The DFT calculations indicated that total energy of the optimized structure of **1** in the $S = 1$ spin state is 0.66 eV (5300 cm$^{-1}$) higher than the energy of the optimized structure of **1** in the $S = 2$ state, in agreement with the experimentally observed $S = 2$ ground-state configuration for **1**. As observed for the other $S = 1$ Fe$^{IV}$ complexes, the Fe–oxo bond lengths for the two DFT-optimized structures are close (1.680 vs 1.706 Å).[10,13,43] However, the Fe–$N_{eq}$ bond lengths differ significantly, indicating that the equatorial ligands play a role in determining the spin state, as suggested by previous studies.[44]

The Mulliken spin on the oxo ligand from DFT ($\rho_p^{DFT}$) is 0.38. This value is significantly lower than the value of 0.56 determined from the experimental $^{17}$O hyperfine constant. The difference between these numbers may reflect underestimation of the spin polarization by DFT or a magnitude of $a_p^{S=1/2}$ that is too small. The $\rho_p^{DFT}$ value of 0.38 for **1** is significantly lower than the reported DFT values of 0.63 for [Fe$^{IV}$(TMG$_3$tren)(O)]$^{2+}$ and 0.6 for TauD-**J**.[14,45] While spin populations calculated from DFT may depend on the functional and basis set used, this dependence is not the cause for the difference, as the calculation for [Fe$^{IV}$(TMG$_3$tren)(O)]$^{2+}$ and **1** used the same functional and basis set. The [Fe$^{IV}$(TMG$_3$tren)(O)]$^{2+}$ complex with similar $C_3$


dx.doi.org/10.1021/ja303224p | J. Am. Chem. Soc. 2012, 134, 9775–9784

symmetry and nitrogen-based equatorial ligands would be expected to have a similar spin polarization of the oxo ligand as in **1**. However, $[Fe^{IV}(TMG_3tren)(O)]^{2+}$ lacks the intramolecular H-bonding network provided by the butylureaylato arms of the $[H_3buea]^{3-}$ ligand. These H-bonds would have the propensity to lower the spin density on the oxo ligand, which may be reflected by the smaller magnitude of $\rho_p^{DFT}$ in **1** relative to $[Fe^{IV}(TMG_3tren)(O)]^{2+}$. The effect of H-bonding is also consistent with the observed lengthening of the Fe−O bond in **1** (1.68 Å) relative to that in $[Fe^{IV}(TMG_3tren)(O)]^{2+}$ (1.65 Å). A similar EPR study of $[Fe^{IV}(TMG_3tren)(O)]^{2+}$ would be useful to corroborate the DFT prediction that $[Fe^{IV}(TMG_3tren)(O)]^{2+}$ has a larger value of $^{17}O A_{iso}$.

TD-DFT calculations were performed to obtain a theoretical value for the zero-field splitting of **1**. The first four excited electronic configurations having $S = 2$ electronic spin are two degenerate pairs at 1.5 and 3.0 eV above the ground $S = 2$ state, as shown in Figure 9. These excited configurations are due to the promotion of an electron from the $d_{x^2-y^2}/d_{xy}$ (1.5 eV) and $d_{xz}/d_{yz}$ (3.0 eV) orbitals to the unoccupied $d_{z^2}$ orbital. The matrix elements of the angular momentum operator (**L**) between $d_{z^2}$ and $d_{x^2-y^2}/d_{xy}$ vanish, and consequently, the $^5E$ configuration at 1.5 eV does not contribute to the **D** tensor. For the $^5E$ configuration at 3.0 eV, however, the matrix elements of **L** between $d_{z^2}$ and $d_{xz}/d_{yz}$ are nonzero, and this configuration contributes to the **D** tensor.

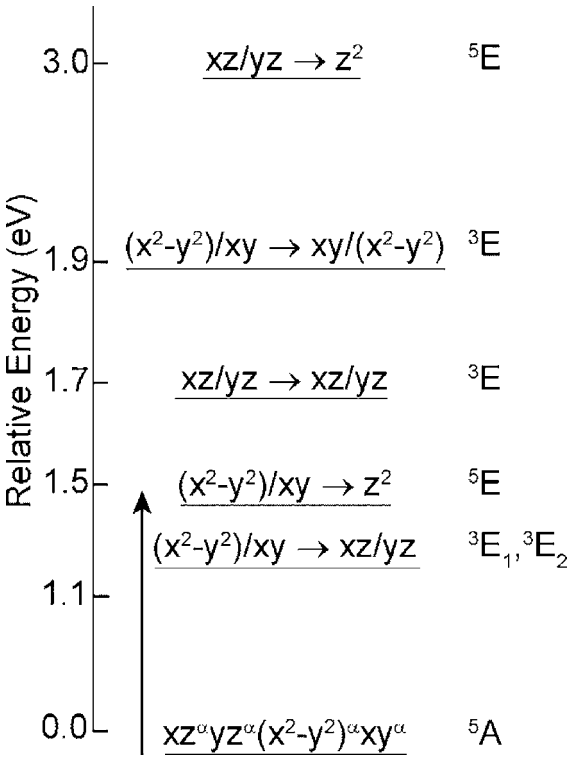


**Figure 9.** Relative energies of quintet and triplet electronic excited states of **1** from TD-DFT and vertical SCF calculations. The orbitals connected by horizontal arrows indicate the d−d electronic transition with respect to the ground-state configuration. The vertical arrow represents the electronic transition observed in optical spectra near 800 nm.

The triplet spin configurations may also contribute to the **D** tensor. The lowest triplet configuration, calculated by computing the SCF energy for a vertical excitation from the ground state, is 1.1 eV higher in energy than the quintet ground state. The TD-DFT calculations revealed four triplet states near this energy arising from the transitions given in Figure 9. In addition, there are excitations to two other pairs of triplet states at 1.7 and 1.9 eV. With the excitation energies calculated using TD-DFT, a theoretical $D$ value was computed as described in the Supporting Information. The computed contributions to the $D$ value from the $S = 2$ and $S = 1$ spin states are $D_2 = +0.73$ cm$^{-1}$ and $D_1 = +3.2$ cm$^{-1}$, respectively, giving a total value of $D = D_1 + D_2 = +3.9$ cm$^{-1}$. The calculated zero-field splitting is in reasonable agreement with the experimental value of +4.7 cm$^{-1}$. The **D** tensors for low-spin ($S = 1$) $Fe^{IV}$ complexes have been shown to have contributions from the $S = 2$ electronic excited states.[46] Notably, the calculations here also demonstrate that the $S = 1$ excited electronic states make major contributions to the $D$ value of **1**. A similar effect of excited-state contributions to the $D$ value due to spin-state mixing was also observed for $Fe^{IV}(H_2O)_5(O)$.[12]

The first quintet excited state appears at an energy of 12 000 cm$^{-1}$ (1.5 eV) above the ground state (Figure 9, marked with an arrow). This energy gap corresponds to a wavelength of 800 nm for a spin-allowed d−d electronic transition ($^5A$ to $^5E$). The electronic absorption spectrum of **1** shows a broad absorbance at 808 nm with $\varepsilon = 280$ M$^{-1}$cm$^{-1}$. The extinction coefficient is in the range expected for d−d transitions.[14] A similar absorbance was observed in the $[Fe^{IV}(TMG_3tren)(O)]^{2+}$ complex at 866 nm, and this complex has a similar $D$ value (+5 cm$^{-1}$). On the basis of this comparison, this absorbance is assigned to the d−d transition between the ground state and the first excited quintet state.

**Spectroscopic Properties of 2 and 2-OH.** The isotropic $^{57}$Fe $A$ value for **2** ($A_{iso} = -24.9$ MHz) is lower than that of **2-OH** (−27.0 MHz) and other characterized ferric complexes. The lower magnitude is due to increased covalency of the Fe−O bond in **2**, which reduces the spin polarization of the s electrons. Such an effect has been reported for other ferric states with significant covalent interactions (e.g., rubredoxin).[47] The covalency of the metal−ligand bonds also affects the magnitude of the isomer shift ($\delta$). For both complexes, the three deprotonated nitrogen atoms of the $[H_3buea]^{3-}$ ligand afford strong in-plane Fe−N bonds, resulting in lower $\delta$ values than commonly observed for ferric complexes. The quadrupole splitting for **2** ($\Delta E_Q = -1.54$ mm/s) is larger in magnitude than $\Delta E_Q$ for **2-OH** (−0.87 mm/s), indicating a larger EFG for the stronger oxo ligand than for the hydroxo ligand. This is consistent with the longer Fe−O bond of **2-OH** (1.931 Å for **2-OH** vs 1.813 Å for **2**). The theoretical values of $\delta$ and $\Delta E_Q$ for these complexes obtained from DFT calculations are in reasonable agreement with the experimental results. The magnitude of $\eta$ for the complex is close to 1 ($\eta^{exptl} = 0.65$, $\eta^{DFT} = 0.72$), and thus, the sign of the quadrupole splitting is indeterminate for **2-OH**.

Simulations of the $^{17}$O isotopic broadening observed in the EPR spectrum of **2-OH** gave $^{17}\mathbf{A}$ = (n.d., ±8, ±12) MHz (Figure 7). This effect is similar to the broadening observed in other water-ligated ferric heme complexes.[48] The $A_x$ value and the signs of these values cannot be determined from the data. The dipolar contribution to the hyperfine tensor determined from DFT calculations was $^{17}\mathbf{A}_{dip}$ = (5.25, −0.35, −4.90) MHz. From the two possible $^{17}\mathbf{A}$ experimental values and the $^{17}\mathbf{A}_{dip}$ tensor from DFT calculations, two possible isotropic values were calculated from eq 3: $^{17}A_{iso} = +8.4$ or −7.6 MHz. The $^{17}A_{iso}$ value of +8.4 MHz can be discarded since the sign of the Fermi


dx.doi.org/10.1021/ja303224p | J. Am. Chem. Soc. 2012, 134, 9775−9784

contact term for $^{17}O$ is negative.[49] From eq 3, the total spin density on the hydroxo ligand was found to be $\rho_p = 0.32$. $Fe^{III}$ has three singly occupied orbitals that interact with the oxygen p orbitals, so the percent delocalization of the spin density for the Fe−OH bond is $(\rho_p/3) \times 100\% = 11\%$. As expected, the spin polarization of the Fe−hydroxo single bond in **2-OH** is lower than that of the Fe−oxo double bond in **1**.

The Fe−O bond in **2** is stronger than the Fe−OH bond in **2-OH** and would be expected to show a larger effect from $^{17}O$ labeling. However, this effect could not be detected in the present samples of **2** for the following reason. For **2**, the simulations required an excessive phenomenological broadening that cannot be attributed to distributions in the zero-field parameters. The crystal structure of **2** shows a closest-packed intermolecular Fe distance of 10 Å. A magnetic dipolar interaction between two $S = {}^5/_2$ molecules (with the zero-field parameters of **2**) that are 10 Å apart should result in signal shifts of up to 14 mT. This shift is comparable to the phenomenological broadening used in the simulation in Figure 5B, indicating short-range aggregation of **2** in frozen solution. We considered a variety of solvent systems to remove the intermolecular interactions, including DMA, DMF, acetonitrile, and THF. The best results were observed for the glass-forming solvent mixture 1:1 DMA/THF. This mixture gave extremely sharp lines for **2-OH**, and while it significantly sharpened the signals for **2**, the dipolar broadening from intermolecular interactions still overwhelmed the expected broadening from isotopic labeling.

Complexes **2** and **2-OH** also display a large change in symmetry, from nearly axial to highly rhombic, as indicated by the change in $E/D$. The low symmetry of **2-OH** is expected, but there are two possible causes for this lower symmetry: (1) a differential interaction of the lone pairs on the hydroxo ligand with the metal d orbitals and (2) a distortion of the urea arms caused by steric interactions with the hydroxo ligand. A similar low symmetry was observed for the $Fe^{III}$−OH complex {[tris(*N*-isopropylcarbamoylmethyl)aminato](hydroxo)ferrate(III)}.[27] This complex does not have the urea arms, and no steric interactions with the hydroxo ligand are present, suggesting that the differential interaction of the hydroxo lone pairs is the dominant reason for the observed lower symmetry.

## CONCLUSION

The present work demonstrates the detection and quantitative characterization of the high-spin $[Fe^{IV}H_3buea(O)]^-$ complex and associated ferric complexes using EPR and Mössbauer spectroscopies. $^{17}O$ EPR studies of $[Fe^{IV}H_3buea(O)]^-$ gave $^{17}O A_{iso} = -16.8$ MHz and a quantitative determination of the spin polarization ($\rho_p = 0.56$) of the oxo p orbitals. The magnitude of the spin polarization is indicative of significant covalency in the Fe−oxo bond, although this is apparently mitigated by the H-bonds between the oxo ligand and the butylureaylato arms of the $[H_3buea]^{3-}$ ligand. The experimental values of the zero-field parameter $D$ for $[Fe^{IV}H_3buea(O)]^-$ and the dipolar $^{57}Fe$ **A** tensors were found to be in good agreement with DFT calculations.

## ASSOCIATED CONTENT

### Supporting Information

Calculations of the $D$ value from the excited-state energies, a figure showing contour plots of Fe-based d orbitals, and distribution of the zero-field splitting. This material is available free of charge via the Internet at http://pubs.acs.org.

## AUTHOR INFORMATION


### Corresponding Author

hendrich@andrew.cmu.edu


### Notes

The authors declare no competing financial interest.

## ACKNOWLEDGMENTS

The authors acknowledge the NIH (GM77387 to M.P.H.; GM50781 to A.S.B.) and an Astrid and Bruce McWilliams Fellowship (R.G.) for financial support. Additional support came from NSF grant CHE070073 to E.L.B. through TeraGrid resources provided by the NCSA and PSC.

## REFERENCES


(1) Borovik, A. S. *Chem. Soc. Rev.* **2011**, *40*, 1870.
(2) Stone, K. L.; Borovik, A. S. *Curr. Opin. Chem. Biol.* **2009**, *13*, 114.
(3) Green, M. T. *Curr. Opin. Chem. Biol.* **2009**, *13*, 84.
(4) Que, L., Jr.; Tolman, W. B. *Nature* **2008**, *455*, 333.
(5) Sono, M.; Roach, M. P.; Coulter, E. D.; Dawson, J. H. *Chem. Rev.* **1996**, *96*, 2841.
(6) Matthews, M. L.; Krest, C. M.; Barr, E. W.; Vaillancourt, F. H.; Walsh, C. T.; Green, M. T.; Krebs, C.; Bollinger, J. M. *Biochemistry* **2009**, *48*, 4331.
(7) Krebs, C.; Fujimori, D. G.; Walsh, C. T.; Bollinger, J. M. *Acc. Chem. Res.* **2007**, *40*, 484.
(8) Fujimori, D. G.; Barr, E. W.; Matthews, M. L.; Koch, G. M.; Yonce, J. R.; Walsh, C. T.; Bollinger, J. M.; Krebs, C.; Riggs-Gelasco, P. J. *J. Am. Chem. Soc.* **2007**, *129*, 13408.
(9) Price, J. C.; Barr, E. W.; Tirupati, B.; Bollinger, J. M.; Krebs, C. *Biochemistry* **2003**, *42*, 7497.
(10) Rohde, J.-U.; In, J.-H.; Lim, M. H.; Brennessel, W. W.; Bukowski, M. R.; Stubna, A.; Münck, E.; Nam, W.; Que, L., Jr. *Science* **2003**, *299*, 1037.
(11) Chanda, A.; Shan, X.; Chakrabarti, M.; Ellis, W. C.; Popescu, D. L.; de Oliveira, F. T.; Wang, D.; Que, L., Jr.; Collins, T. J.; Münck, E.; Bominaar, E. L. *Inorg. Chem.* **2008**, *47*, 3669.
(12) Pestovsky, O.; Stoian, S.; Bominaar, E. L.; Shan, X.; Münck, E.; Que, L., Jr.; Bakac, A. *Angew. Chem., Int. Ed.* **2005**, *44*, 6871.
(13) Lacy, D. C.; Gupta, R.; Stone, K. L.; Greaves, J.; Ziller, J. W.; Hendrich, M. P.; Borovik, A. S. *J. Am. Chem. Soc.* **2010**, *132*, 12188.
(14) England, J.; Martinho, M.; Farquhar, E. R.; Frisch, J. R.; Bominaar, E. L.; Münck, E.; Que, L., Jr. *Angew. Chem., Int. Ed.* **2009**, *48*, 3622.
(15) Bigi, J. P.; Harman, W. H.; Lassalle-Kaiser, B.; Robles, D. M.; Stich, T. A.; Yano, J.; Britt, R. D.; Chang, C. J. *J. Am. Chem. Soc.* **2012**, *134*, 1536.
(16) MacBeth, C. E.; Golombek, A. P.; Young, V. G., Jr.; Yang, C.; Kuczera, K.; Hendrich, M. P.; Borovik, A. S. *Science* **2000**, *289*, 938.
(17) Bernasconi, L.; Louwerse, M. J.; Baerends, E. J. *Eur. J. Inorg. Chem.* **2007**, 3023.
(18) Decker, A.; Rohde, J.-U.; Klinker, E. J.; Wong, S. D.; Que, L., Jr.; Solomon, E. I. *J. Am. Chem. Soc.* **2007**, *129*, 15983.
(19) Hirao, H.; Kumar, D.; Que, L., Jr.; Shaik, S. *J. Am. Chem. Soc.* **2006**, *128*, 8590.
(20) Shaik, S.; Hirao, H.; Kumar, D. *Acc. Chem. Res.* **2007**, *40*, 532.
(21) Ye, S.; Neese, F. *Curr. Opin. Chem. Biol.* **2009**, *13*, 89.
(22) Janardanan, D.; Wang, Y.; Schyman, P.; Que, L., Jr.; Shaik, S. *Angew. Chem., Int. Ed.* **2010**, *49*, 3342.
(23) Geng, C.; Ye, S.; Neese, F. *Angew. Chem., Int. Ed.* **2010**, *49*, 5717.
(24) Shaik, S.; Chen, H.; Janardanan, D. *Nat. Chem.* **2011**, *3*, 19.
(25) Seo, M. S.; Kim, N. H.; Cho, K.-B.; So, J. E.; Park, S. K.; Clemancey, M.; Garcia-Serres, R.; Latour, J.-M.; Shaik, S.; Nam, W. *Chem. Sci.* **2011**, *2*, 1039.
(26) Manner, V. W.; Lindsay, A. D.; Mader, E. A.; Harvey, J. N.; Mayer, J. M. *Chem. Sci.* **2012**, *3*, 230.
(27) Mukherjee, J.; Lucas, R. L.; Zart, M. K.; Powell, D. R.; Day, V. W.; Borovik, A. S. *Inorg. Chem.* **2008**, *47*, 5780.

(28) Ehrensberger, K.; Schmalle, H. W.; Oswald, H.; Reller, A. *J. Therm. Anal. Calorim.* **1999**, *57*, 139.
(29) Stolt, M.; Södergård, A. *Macromolecules* **1999**, *32*, 6412.
(30) Petasis, D. T.; Hendrich, M. P. *J. Magn. Reson.* **1999**, *136*, 200.
(31) Golombek, A. P.; Hendrich, M. P. *J. Magn. Reson.* **2003**, *165*, 33.
(32) Frisch, M. J.; et al. *Gaussian 03*, revision E.01; Gaussian, Inc.: Wallingford, CT, 2004.
(33) Vrajmasu, V.; Münck, E.; Bominaar, E. L. *Inorg. Chem.* **2003**, *42*, 5974.
(34) MacBeth, C. E.; Gupta, R.; Mitchell-Koch, K. R.; Young, V. G., Jr.; Lushington, G. H.; Thompson, W. H.; Hendrich, M. P.; Borovik, A. S. *J. Am. Chem. Soc.* **2004**, *126*, 2556.
(35) Hendrich, M. P.; Debrunner, P. G. *Biophys. J.* **1989**, *56*, 489.
(36) The value for this complex was calculated from the two experimental *A* values and the dipolar **A** tensor from DFT calculations
(37) Mbughuni, M. M.; Chakrabarti, M.; Hayden, J. A.; Bominaar, E. L.; Hendrich, M. P.; Münck, E.; Lipscomb, J. D. *Proc. Natl. Acad. Sci. U.S.A.* **2010**, *107*, 16788.
(38) Astashkin, A. V.; Neese, F.; Raitsimring, A. M.; Cooney, J. J. A.; Bultman, E.; Enemark, J. H. *J. Am. Chem. Soc.* **2005**, *127*, 16713.
(39) Melamud, E.; Silver, B. L. *J. Phys. Chem.* **1973**, *77*, 1896.
(40) Morton, J. R.; Preston, K. F. *J. Magn. Reson.* **1978**, *30*, 577.
(41) Roberts, J. E.; Hoffman, B. M.; Rutter, R.; Hager, L. P. *J. Am. Chem. Soc.* **1981**, *103*, 7654.
(42) Chiesa, M.; Giamello, E.; Paganini, M. C. *J. Chem. Phys.* **2002**, *116*, 4266.
(43) England, J.; Guo, Y.; Farquhar, E. R.; Young, V. G., Jr.; Münck, E.; Que, L., Jr. *J. Am. Chem. Soc.* **2010**, *132*, 8635.
(44) Neese, F. *J. Inorg. Biochem.* **2006**, *100*, 716.
(45) Sinnecker, S.; Svensen, N.; Barr, E. W.; Ye, S.; Bollinger, J. M.; Neese, F.; Krebs, C. *J. Am. Chem. Soc.* **2007**, *129*, 6168.
(46) Schoneboom, J. C.; Neese, F.; Thiel, W. *J. Am. Chem. Soc.* **2005**, *127*, 5840.
(47) Yoo, S. J.; Meyer, J.; Achim, C.; Peterson, J.; Hendrich, M. P.; Münck, E. *J. Biol. Inorg. Chem.* **2000**, *5*, 475.
(48) Fittipaldi, M.; García-Rubio; Trandafir, F.; Gromov, I.; Schweiger, A.; Bouwen, A.; Doorslaer, S. V. *J. Phys. Chem. B* **2008**, *112*, 3859.
(49) Hermosilla, L.; Calle, P.; García de la Vega, J. M.; Sieiro, C. *J. Phys. Chem. A* **2005**, *109*, 1114.